J. Fluid Mech. (1982), *vol.* 114, *pp.* 213–236
Printed in Great Britain

Submerged laminar jet impingement on a plane

By MOHAN D. DESHPANDE
Department of Mechanical Engineering, The Catholic University of America, Washington, D.C. 20064

AND RAMESH N. VAISHNAV
Department of Civil Engineering, The Catholic University of America, Washington, D.C. 20064

(Received 3 June 1980 and in revised form 10 March 1981)

Submerged laminar jet impingement on a plane is studied using computation. Steady-state Navier–Stokes equations for the axisymmetric case are solved numerically. The extent of the infinite flow is approximated by applying the boundary conditions at a finite but sufficiently large distance. The tube-exit velocity profile is assumed to be either a fully developed parabolic profile or a flat profile. For the former case, two different nozzle heights from the target plane are considered. The presence of a toroid-shaped eddy at low values of Reynolds number, *Re*, leads to some interesting observations such as the manner in which the wall shear stress depends on *Re*. An increase in the height of the nozzle exit from the target plane decreases the wall shear stress, more so at lower values of *Re*. A change from the parabolic exit velocity profile to the flat profile leads to a decrease in wall shear stress due to decreased momentum flux. The study was motivated by experiments designed to measure the yield shear strength of the vascular endothelium wherein a small saline jet was used to erode the tissue by normal impingement.

1. Introduction

In this communication we present the details of the flow field arising in a body of fluid when a submerged, axisymmetric laminar jet impinges normally on a rigid plane. The Navier–Stokes equations for this case have been solved numerically. The motivation for this problem came from some of our studies (see, for example, Vaishnav, Atabek & Patel 1978) in which we used submerged laminar jets of saline impinging on the endothelial surface of a vascular tissue to study the shear strength of this delicate layer of cells, which is of considerable importance in the study of atherogenesis (Fry 1973).

The problem of a fluid jet impinging on a surface is also of considerable technological importance. Examples are: hydraulic outlet works; vertical-take-off aircraft; paint sprays and jet cooling. However, in most applications the flows are turbulent, and consequently most of the work in this area is concerned with turbulent jets only, although some studies on laminar jets are also available.

Previous investigators have identified three regions of distinct flow characteristics (figure 1) in both laminar and turbulent cases: (1) the free-jet region, in which the flow is not influenced significantly by the surface of impingement and the dominant velocity component is axial; (2) the wall-jet region, in which the dominant velocity component is radial and in which the boundary layer is subject to nearly zero pressure gradient, and thickens as one moves radially outward; (3) the impingement region, which lies between the other two, which is characterized by significant changes in flow direction. Most analytical studies have concentrated on the flow field in the wall jet region. Most experimental studies appear to have been carried out in the impingement region. Our interest here is to characterize the entire flow field.

The laminar plane wall-jet was first studied theoretically by Tetervin (1948). Glauert (1956) solved the boundary layer equations analytically for the plane and axisymmetric cases, and obtained similarity solutions for these problems. He showed that for the axisymmetric problem the radial component of the velocity, the boundary-layer thickness, and the shear stress at the wall, are proportional to the $-\frac{3}{2}, \frac{5}{4}$, and $-\frac{11}{4}$ powers of the radial distance from the stagnation point, respectively. It should be pointed out that Glauert's solution is valid only at distances far away from the stagnation point and that the solution involves a constant which needs to be determined from other considerations. Bajura & Szewczyk (1970) verified Glauert's solution experimentally. A second-order correction to Glauert's similarity solution was given by Plotkin (1970).

The case of inviscid two-dimensional jet impingement was treated by Strand (1962). Ojha & Gollakota (1977) solved the boundary-layer equations to study the impingement over a curved surface. van Heiningen, Mujumdar & Douglas (1976) and Saad, Douglas & Mujumdar (1977) obtained the flow field and heat transfer characteristics numerically for two-dimensional and axisymmetric laminar impinging jets, respectively, when the flow is confined between two parallel plates.

Among the works on turbulent jets we may cite the following. Bakke (1957), Bradshaw & Love (1961), Tani & Komatsu (1964), Poreh, Tsuei & Cermak (1967), Bradbury (1972), and Beltaos & Rajaratnam (1974) studied turbulent axisymmetric jet impingement experimentally. Wolfshtein (1970) used a mixing length model to compute the solution for a plane turbulent impingement jet numerically. Kamoi & Tanaka (1972) conducted experiments with oblique impingement. Gardon & Akfirat (1966) and Baines & Keffer (1976) studied heat transfer under two-dimensional turbulent jet impingement.

It seems that no study is available wherein the complete flow field for a laminar jet impingement in an unbounded medium is computed. In this study we consider the case of jet impingement in an unbounded medium and compute the flow field in the body of the fluid in which the jet is submerged. The far-field asymptotic form of the flow field is simulated by applying numerical boundary conditions at a finite, but significantly large, distance away from the impingement region.

2. Governing equations and boundary conditions

Figure 1 shows schematically a cylindrical tube of radius a_0 with its exit end located at a height h above a flat surface. We consider the flow field induced by a fluid jet issuing from the tube and impinging on to the flat surface. We assume that the jet is submerged, the fluid is of infinite extent, the flow is axially symmetric, and the tube is of infinite length and zero thickness. We employ a cylindrical co-ordinate system (r, θ, z) shown in figure 1 to describe the flow field.

If we assume that the flow is steady and laminar, and the fluid is incompressible and

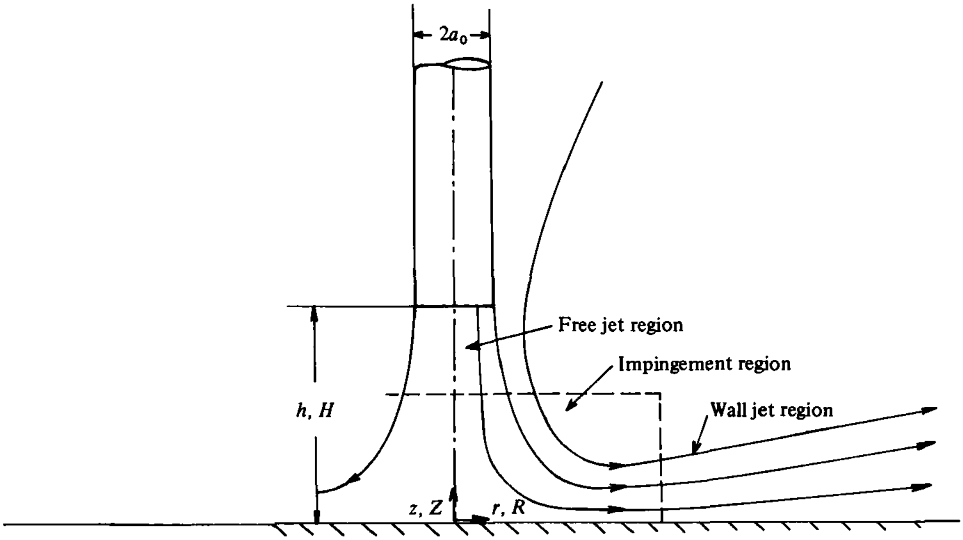

FIGURE 1. Flow configuration.

Newtonian, then the governing differential equations are the Navier–Stokes equations and the continuity equation (Schlichting 1979). If we use vorticity and stream function as the dependent variables, these equations reduce to

$$\omega = -\frac{1}{R}\left(\frac{\partial^2\psi}{\partial R^2}+\frac{\partial^2\psi}{\partial Z^2}\right)+\frac{1}{R^2}\frac{\partial\psi}{\partial R}, \tag{1}$$

$$R^2\left[\frac{\partial}{\partial Z}\left(\frac{\omega}{R}\frac{\partial\psi}{\partial R}\right)-\frac{\partial}{\partial R}\left(\frac{\omega}{R}\frac{\partial\psi}{\partial Z}\right)\right]-\frac{1}{Re}\frac{\partial}{\partial Z}\left[R^3\frac{\partial}{\partial Z}\left(\frac{\omega}{R}\right)\right]-\frac{1}{Re}\frac{\partial}{\partial R}\left[R^3\frac{\partial}{\partial R}\left(\frac{\omega}{R}\right)\right]=0, \tag{2}$$

where $R = r/a_0$ and $Z = z/a_0$ are the non-dimensional co-ordinates, v_r and v_z are the radial and axial velocity components, $V_R = v_r/2\bar{u}$ and $V_Z = v_z/2\bar{u}$ are the corresponding velocity components, non-dimensionalized with respect to $\bar{u}$, the average velocity at the tube exit plane.

In the above, $\omega = \partial V_R/\partial Z - \partial V_Z/\partial R$ is the non-dimensional vorticity, ψ is the non-dimensional stream function such that $V_Z = R^{-1}\,\partial\psi/\partial R$ and $V_R = -R^{-1}\,\partial\psi/\partial Z$, and $Re = 2\bar{u}a_0/\nu$ is the Reynolds number in which ν is the kinematic viscosity. Other quantities of interest are ρ, the fluid density, $H = h/a_0$, the non-dimensional height of the tube exit above the flat surface, and $P = p/(4\rho\bar{u}^2)$, the non-dimensional pressure. Solution of the problem consists of solving differential equations (1) and (2) subject to the boundary conditions described below.

At infinity, the velocity components go to zero asymptotically. For the numerical solution of the problem we apply appropriate boundary conditions at the boundaries AF and FE in figure 2, so that the flow field at infinity is sufficiently well approximated. The boundary conditions applied on CD and the five surfaces CB, AB, DE, AF and FE are as follows.

(*a*) *On the axis CD*. Because of axial symmetry, $V_R = 0$, $\omega = 0$, $\psi =$ constant on CD. Without loss of generality, we take $\psi = 0$ on CD. However, $\omega/R \neq 0$ on CD, but can be evaluated as follows. Assume that ψ is of the form,

$$\psi = a(Z)\,R^2 + b(Z)\,R^4 \tag{3}$$

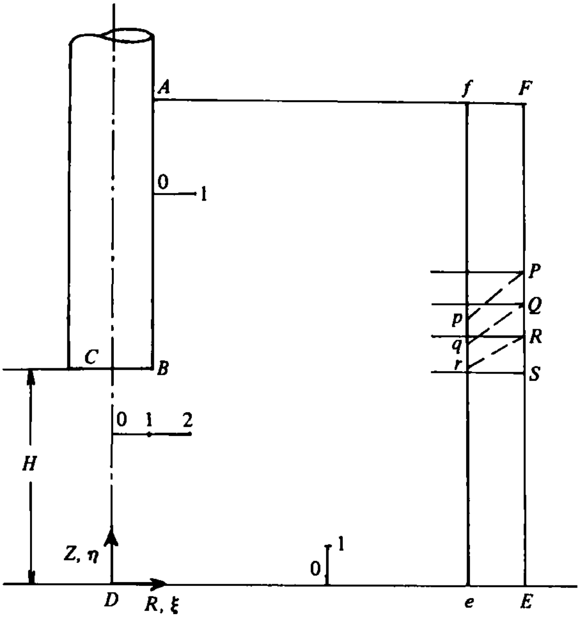

FIGURE 2. Boundary conditions.

in the neighbourhood of CD, where $a(Z)$ and $b(Z)$ are functions of Z only. At a given value of Z, $\psi = a(Z)\,R^2 + b(Z)\,R^4$. By substituting this form of ψ in (1), the value of ω/R at $Z = Z_0$ can be expressed as

$$\left.\frac{\omega}{R}\right|_{Z=Z_0} = -8b - \frac{\partial^2 a}{\partial Z^2}. \tag{4}$$

The values of $b(Z)$ and $a(Z)$ in (3) can be obtained as

$$b(Z) = \frac{1}{R_2^2 - R_1^2}\left(\frac{\psi_2}{R_2^2} - \frac{\psi_1}{R_1^2}\right),$$

$$a(Z) = \frac{1}{R_2^2 - R_1^2}\left(\frac{R_2^2}{R_1^2}\psi_1 - \frac{R_1^2}{R_2^2}\psi_2\right),$$

in terms the values ψ_1 and ψ_2 of ψ at the nodal points (R_1, Z) and (R_2, Z), respectively (see figure 2).

(*b*) *On tube exit plane CB.* On this plane, velocity V_Z is assumed to have a parabolic, fully developed profile, $R^2 - 1$. Also, $\psi|_{CB} = -\frac{1}{2}R^2 + \frac{1}{4}R^4$ and $(\omega/R)_{CB} = -2$. Some cases with a nearly flat velocity profile were also considered. For a truly flat velocity profile $\psi|_{CB} = -\frac{1}{4}R^2$, and $\omega/R = 0$, except at the lip of the tube ($R = 1$) where $\omega/R \rightarrow \infty$. To avoid this difficulty of specifying ω/R at $R = 1$, a profile with almost constant velocity was taken with $V_Z = 5(R^{18} - 1)/9$, for which $\psi = R^{20}/36 - 10R^2/36$, and $\omega/R = -10R^{16}$.

(*c*) *On the tube wall AB.* On this surface, the 'no-slip' boundary condition is applied. The manner in which the problem has been non-dimensionalized, leads to $\psi = -\frac{1}{4}$, regardless of the exit velocity profile at CB. Vorticity ω is unknown on AB. It can be approximated as follows. We first expand ψ and ω in Taylor series in R at $R = 1$, for a given value of Z. We then set the derivatives $(\partial\psi/\partial R)|_{R=1}$ and $(\partial^n\psi/\partial Z^n)|_{R=1}$ for all n

and Z equal to zero in the series for ψ to account for the 'no-slip' boundary condition at $R = 1$. In addition, we use the governing equation (1) which leads to

$$\omega_0 R_0 = \frac{-\Delta\psi(6/l^2) - \omega_1 R_1}{2 + (l/R_0) - (l^2/4R_0^2)} + O(l^3), \tag{5}$$

where $\Delta\psi = \psi_1 - \psi_0$, $l = R_1 - R_0 = R_1 - 1$ and the suffixes 0 and 1 correspond to the nodal points 0 on the wall and 1 the adjacent nodal point in the radial direction (see figure 2). Details may be obtained from Lester (1961) or Deshpande, Giddens & Mabon (1976).

(*d*) *On wall DE.* 'No-slip' boundary condition is applied on this surface and the value of ψ is taken to be zero. A procedure similar to that used for the wall AB yields

$$\omega_0 = \frac{-\Delta\psi(6/k^2) - \omega_1 R}{2R} + O(k^3), \tag{6}$$

where $\Delta\psi = \psi_1 - \psi_0$ and $k = Z_1 - Z_0 = Z_1$.

(*e*) *On boundary AF.* As $Z \to \infty$, $V_R \to 0$ and $V_Z \to 0$. However, these boundary conditions cannot be applied in a numerical scheme and appropriate boundary conditions must be applied at a finite distance. Therefore, on the boundary AF, which is located at a distance of 10 tube radii away from the plane of impingement, we use the boundary conditions

$$\frac{\partial^2\psi}{\partial Z^2} = 0, \quad \frac{\partial\omega}{\partial Z} = 0. \tag{7}$$

The first of these boundary conditions implies that $\partial V_R/\partial Z = 0$.

(*f*) *On boundary FE.* As $R \to \infty$, $V_R \to 0$ and $V_Z \to 0$. Again, we must simulate these conditions by applying boundary conditions at FE which is located at a finite distance of 10 tube radii from the tube axis. It is not satisfactory to assume that the gradients of ψ and ω in the radial direction go to zero on the boundary FE. We therefore have developed a method to formulate the boundary conditions which employs a weak form of Glauert's similarity solution.

In this procedure, information from line fe is employed to determine ψ and ω/R values on line FE, i.e. at nodal points P, Q, R, S, etc. (figure 2). Since the similarity solution due to Glauert contains an unknown constant, it cannot be used directly to determine the ψ and ω values on line FE in terms of conditions at the tube exit plane CB. However, the flow quantities at a typical point Q on line FE and at the corresponding similarity point q on line fe can be related explicitly in terms of their radial locations, R_Q and R_q, respectively. The flow quantities on line fe are taken from the solution at the previous level of iteration and hence are exact only when the solution converges.

The distance from the wall, η_1, in the similarity solution is proportional to $R^{-\frac{5}{4}}Z$. Now, corresponding to the nodal point Q on the line FE, a point q can be selected on the line fe such that both have the same η_1, that is, they correspond to the same point in the similarity solution. Hence the stream function and vorticity in the similarity solution (not ψ and ω as defined in this study) are the same at these points. Using this equality to relate ψ and ω at corresponding points Q and q we can write

$$\psi_Q/\psi_q = (R_Q/R_q)^{\frac{3}{4}}, \tag{8}$$

$$\omega_Q/\omega_q = (R_q/R_Q)^{\frac{11}{4}}, \tag{9}$$

$$(\omega/R)_Q/(\omega/R)_q = (R_q/R_Q)^{\frac{15}{4}}. \tag{10}$$

These relations enable us to calculate ψ and ω/R at point Q from the known values at q. The point q is not a nodal point and a Lagrangian interpolation scheme was used to compute the values at q from the three neighbouring nodal points on line *fe*.

The method was successful except when the distance *eE* was excessively large. (A better way of describing this would be in terms of the ratio R_e/R_E of the radii R_e and R_E.) This is not a serious problem since good numerical accuracy demands a small value of *eE* anyway. The success of the method was proved by comparing the profiles obtained at *FE* with the similarity solution and by moving the boundary *FE* closer to the axis and still being able to reproduce practically the same results. Explicit forms of the similarity solution were not assumed at the boundary *FE*.

3. Numerical solution

To solve the problem numerically, a co-ordinate transformation is used so that the grid points in the transformed plane are distributed uniformly, while providing more points in the physical space where the flow variables such as vorticity and velocities are expected to change rapidly. The transformation used was

$$\xi = \tanh k_1 R, \tag{11}$$

$$\eta = aZ + b(1 - e^{-cZ}), \tag{12}$$

where k_1, a, b, and c are constants. Correspondingly, the governing equations (1) and (2) are transformed to

$$\frac{\partial}{\partial \xi}\left(\frac{M_1}{N_1}\frac{1}{R}\frac{\partial \psi}{\partial \xi}\right) + \frac{\partial}{\partial \eta}\left(\frac{N_1}{M_1}\frac{1}{R}\frac{\partial \psi}{\partial \eta}\right) + \frac{\omega}{M_1 N_1} = 0, \tag{13}$$

$$R_e R^2\left[\frac{\partial}{\partial \eta}\left(\frac{\omega}{R}\frac{\partial \psi}{\partial \xi}\right) - \frac{\partial}{\partial \xi}\left(\frac{\omega}{R}\frac{\partial \psi}{\partial \eta}\right)\right] - \frac{\partial}{\partial \eta}\left[\frac{N_1}{M_1}R^3\frac{\partial}{\partial \eta}\left(\frac{\omega}{R}\right)\right] - \frac{\partial}{\partial \xi}\left[\frac{M_1}{N_1}R^3\frac{\partial}{\partial \xi}\left(\frac{\omega}{R}\right)\right] = 0, \tag{14}$$

where

$$M_1 = \frac{\partial \xi}{\partial R} = k_1(1-\xi^2), \tag{15}$$

$$M_2 = \frac{\partial^2 \xi}{\partial R^2} = -2k_1 \xi M_1, \tag{16}$$

$$N_1 = \frac{\partial \eta}{\partial Z} = a + bce^{-cZ} \tag{17}$$

$$N_2 = \frac{\partial^2 \eta}{\partial Z^2} = -bc^2 e^{-cZ} = c(a - N_1). \tag{18}$$

Equation (11) transforms the line $0 \leqslant R < \infty$ into the line $0 \leqslant \xi < 1$. On the other hand, equation (12) transforms the line $0 \leqslant Z < \infty$ into the line $0 \leqslant \eta < \infty$. For both of the transformations, equidistant intervals in the transformed lines correspond to closely spaced intervals in the physical space near the axis (for R) and near the wall (for Z). From equation (12) we see that for large values of Z, the transformation is approximately linear. The actual values of the constants k_1, a, b, and c to be used in a particular case depend, to a certain extent, on the actual values of *Re* and H. For example, the set of values, $c = 3$, $a \simeq 0.07143$, $b \simeq 0.28572$ and $k_1 \simeq 0.15288$ was found

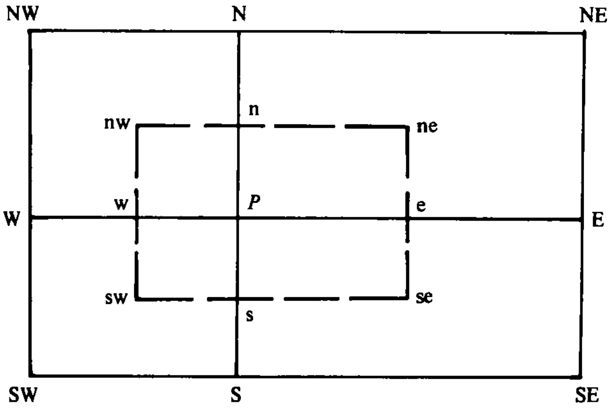

FIGURE 3. Control volume for numerical scheme.

to be satisfactory for $H = 4$ for all values of *Re* used in the present study. Inverting transformation (11) is straightforward, but such is not the case with transformation (12). For a given η, one has to resort to an iterative scheme to compute Z from (12) and simple schemes are likely to fail for small or for large values of η. A Newton–Raphson scheme was used to compute the values of Z corresponding to the nodal values of η.

We may mention here that an earlier numerical scheme employed a hyperbolic tangent transformation similar to (11) in the Z-direction also. It was found to be satisfactory at low values of *Re*; however, numerical experiments proved that the results were unacceptable at high values of *Re*. A switch to transformation (12) was made and the present combination of transformations (11) and (12) proved to give consistently good results.

The transformed equations (13) and (14) together with the boundary conditions were solved numerically using the finite-difference scheme of Gosman *et al.* (1969) with some modifications. Difference equations were generated by integrating the equations over a control volume surrounding a point P (shown by dotted lines in figure 3). Upwind differencing was used to approximate the convection terms. The resulting difference equations express the values of the dependent variables at P in terms of their values at the eight neighbouring nodes N, NE, E, etc. These equations are summarized below.

To simplify writing, equations (13) and (14) are cast in the general form

$$a\left[\frac{\partial}{\partial \eta}\left(\phi\frac{\partial \psi}{\partial \xi}\right)-\frac{\partial}{\partial \xi}\left(\phi\frac{\partial \psi}{\partial \eta}\right)\right]-\frac{\partial}{\partial \xi}\left[b_1 R\frac{\partial}{\partial \xi}(c\phi)\right]-\frac{\partial}{\partial \eta}\left[b_2 R\frac{\partial}{\partial \eta}(c\phi)\right]+Rd = 0, \tag{19}$$

where $\phi = \omega/R$ or ψ. The values of the coefficients a, b_1, etc. are listed in table 1. The final difference equations for ω/R and ψ are

$$\phi_P \sum_j (A_j+B_j) = \sum_j [\phi_j(A_j+B_j)]-V_P\bar{d}_P, \tag{20}$$

where summations are carried out over the four points E, W, N, and S (see figure 3), and the suffix P refers to the nodal point P. A bar over a term represents the average of the term over the control volume. Also,

$$V_P = \tfrac{1}{4}R_P(\eta_N-\eta_S)(\xi_E-\xi_W), \tag{21}$$

$$A_E = \bar{a}_P[(\psi_N+\psi_{NE}-\psi_S-\psi_{SE})+|(\psi_N+\psi_{NE}-\psi_S-\psi_{SE})|]/8 \tag{22}$$

ϕ	a	b_1	b_2	c	d
ω/R	ReR^3	$\frac{M_1}{N_1}R^2$	$\frac{N_1}{M_1}R^2$	1	0
ψ	0	$\frac{M_1}{N_1}\frac{1}{R^2}$	$\frac{N_1}{M_1}\frac{1}{R_2}$	1	$-\frac{\omega/R}{M_1N_1}$

TABLE 1. Coefficients in equation (19).

with similar expressions for A_W, A_N and A_S, and

$$B_E = \frac{b_{1E}+b_{1P}}{8}\frac{R_E+R_P}{\xi_E-\xi_P}(\eta_N-\eta_S) \tag{23}$$

with similar expressions for B_W, B_N and B_S. The two equations represented by (19) were solved using an iterative scheme. In this scheme, an initial guess is made for the flow field and the boundary conditions are imposed. The set of difference equations is then solved for the whole domain of interest by using the latest values of ψ and ω available. The boundary conditions are then recomputed from the latest values of ψ and ω and the process is continued until convergence is obtained. Convergence is tested by comparing the values of ψ and ω from successive iterations and ensuring that the maximum changes in ψ and ω are within preselected tolerances. These tolerances were generally set at 6×10^{-5} and 10^{-5} for ψ and ω/R, respectively.

The vorticity at the tube lip is a discontinuous function and thus it required special consideration. When solving the equations for a point with $R < 1$, the vorticity value at the tube lip was assumed to be the same as the vorticity of the tube exit-velocity profile. For calculations at a point with $R > 1$, the vorticity value at the lip was obtained by calculating it as though the lip were a point on the exterior of the tube wall. For calculations at the points exactly under the lip ($R = 1$), an average of the two values obtained above was employed.

The velocities, pressure and wall shear stress were calculated after the converged solution was obtained. Velocities were obtained from the stream function using the central difference scheme. The radial pressure gradient on the plane wall is

$$\left.\frac{\partial P}{\partial R}\right|_{(\text{wall})} = \frac{1}{Re}\frac{\partial \omega}{\partial Z}. \tag{24}$$

The axial pressure gradient at any point can be calculated from

$$\frac{\partial P}{\partial Z} = V_R\omega - \frac{1}{Re}\left(\frac{\partial \omega}{\partial R}+\frac{\omega}{R}\right) - \left[V_Z\frac{\partial V_Z}{\partial Z} + V_R\omega + V_R\frac{\partial V_Z}{\partial R}\right], \tag{25}$$

and the wall shear stress τ_w (dimensional value) from

$$\tau_w/(4\rho\bar{u}^2) = \omega_w/Re. \tag{26}$$

The solution obtained for a particular value of Re was used as the initial guess for the iterative computations for a higher value of Re. The number of grid points in the radial direction was 61 with 11 points between $R = 0$ and $R = 1$. The number of grid points in the axial direction was 36 with 18 points between $Z = 0$ and $Z = H$. The number of iterations required to get a converged solution varied from 300 to 600. One hundred iterations required about 78 seconds of computer time on the DEC system-10, Model 90, computer at The Catholic University of America.

Various numerical experiments were performed to ensure numerical accuracy of the results. For example, in one experiment, the convergence of the solution was studied. For the case of $H = 4$ and $Re = 1250$, the solution converged after 600 iterations according to the criterion described before. An additional 600 iterations were executed to make sure that the solution obtained did not drift away. In another set of experiments, the effect of grid spacing and the transformation parameters was studied. This was done by (*a*) taking a cruder grid spacing, (*b*) taking a finer grid spacing, and (*c*) varying the constants in the co-ordinate transformation substantially to see if the choice of constants was satisfactory. A third set of experiments was conducted to check how well the boundary conditions applied on FE and AF (figure 2) simulated the conditions at $R = \infty$ and $Z = \infty$, respectively. This was done for the case of $Re = 1000$ by changing the locations of FE and AF. The boundary AF was moved to a height of 20 radii. The boundary FE was moved to 20, 8 and 6 radii distances. The weak form of the similarity solution proved to be applicable at a distance as close as 6 radii. The solution obtained in the similarity region was compared with the solution due to Glauert and the computed solution in the neighbourhood of the stagnation point was compared with the stagnation point flow solution (Schlichting 1979). These comparisons are shown in a later section. The numerical scheme mentioned earlier which used a hyperbolic tangent co-ordinate transformation in the Z-direction did not yield satisfactory results at high Re when subjected to the three checks of accuracy mentioned above and was therefore discarded. On the other hand, the present scheme yielded satisfactory results when subjected to these tests, which enhances our confidence in the results.

4. Results

As noted previously, calculations were performed for two tube exit-velocity profiles and various values of Re and H. For the parabolic velocity profile, the values of $H = 4$ and $H = 3$ were used. For the former case, a range of Re from 0 to 2000 was used and for the latter case a range of Re from 0 to 1500 was used. For the flat velocity profile, a value of $H = 4$ was used with $Re = 1000$, 1500 and 2000.

4.1. *Streamlines and vorticity contours*

A good description of a steady laminar flow is given by a display of the streamlines. Three such displays of streamlines are given in figure 4 for three representative Reynolds numbers. In these cases, the value of H was 4 and the parabolic exit-velocity profile was used. A toroidal eddy can be seen in figure 4(*a*) just above the tube exit level. The nature of the flow at this low value of $Re = 1$ is somewhat different from the three distinct regions indicated earlier in figure 1. Notice that at the $R = 10$ boundary the gradients of ψ in R direction do not go to zero. If the Reynolds number is increased, the eddy is pushed downward (figure 4*b*, $Re = 25$) and also there is an increase in the volume of fluid rotating in this fashion. When the Reynolds number is increased even further (figure 4*c*, $Re = 1000$) the eddy is swept away and we get the three regions of flow discussed in § 1. The flow issuing from the tube is seen to be restricted to a thin region between the wall and the streamline with $\psi = -0{\cdot}25$. At $Re = 100$ the nature

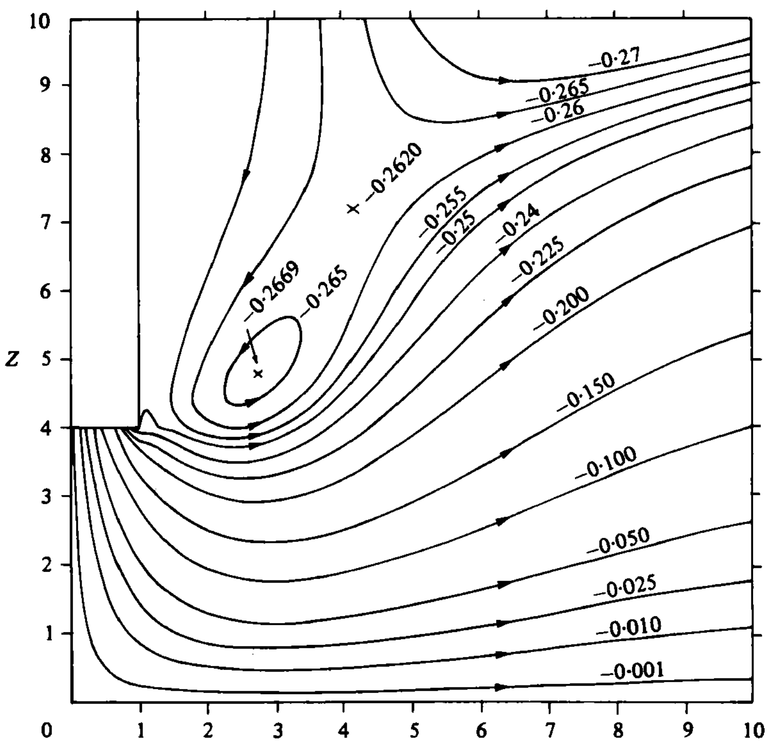

(a)

Caption for figure 4(a) on p. 224.

of the flow is similar to the case of $Re = 1000$ and as may be expected, the boundary layer is thicker.

The vorticity contours are displayed in figure 5 for $H = 4$ and $Re = 1$ and $Re = 100$. It can be seen again clearly that the gradients of the flow quantities do not go to zero at the boundary $R = 10$. This re-emphasizes the need to treat the boundary conditions on FE in the manner described earlier rather than merely setting the gradients of ψ and ω in the R direction to be zero.

The presence of the eddy at low Reynolds numbers has a strong influence on the flow characteristics and hence the locus of the centre of the eddy is indicated in figure 6 for the cases of $H = 3$ and $H = 4$ and the parabolic inlet velocity profile at the tube exit. The Reynolds numbers corresponding to these steady-state solutions are indicated in the figure. A slight increase in Re from zero to two leads to a radially outward shift of the centre of the eddy. An increase from 2 to 25 causes an almost vertically downward shift, with a very slight shift of the centre of the eddy toward the axis. A further increase in Re to 70 causes a radially outward and slightly upward shift. As will be seen later, a large change in flow behaviour takes place close to the wall, under the eddy, when Re is increased from 2 to 25.

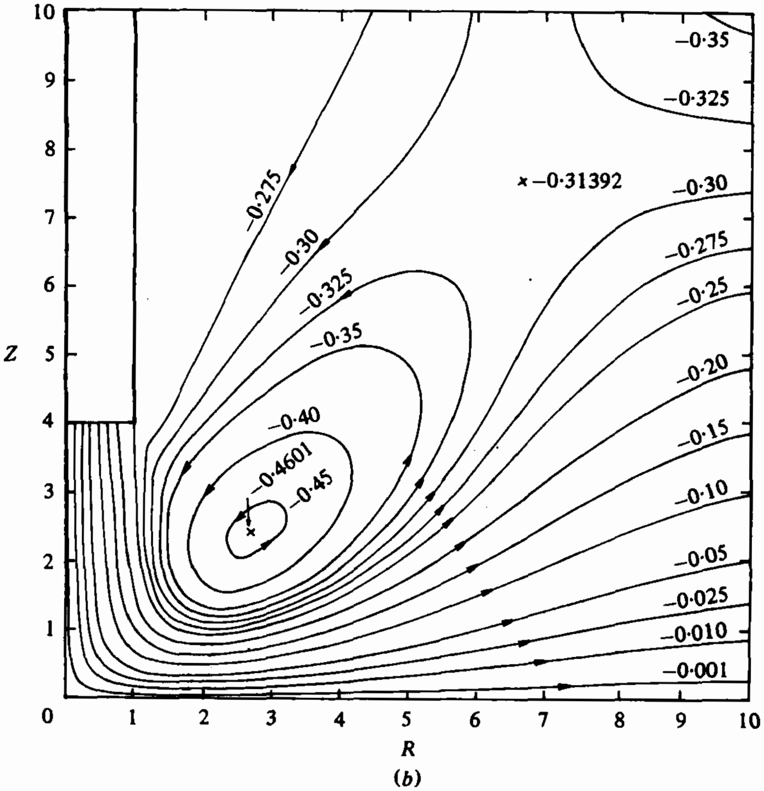

Caption for figure 4(*b*) on p. 224.

4.2. *Velocity profiles*

Radial velocity profiles in figure 7 are shown for several radial locations, R, for the case of $H = 4$. At a low Reynolds number, $Re = 1$ (figure 7*a*), the radial velocity is low everywhere due to viscous diffusive action. The maximum values of velocity occur away from the flat surface and the wall vorticity (non-dimensional) is seen to be small (see figure 5*a*). The radial velocity at the tube exit is positive as can also be seen from the streamline patterns in figure 4(*a*). The picture at a higher Re of 1000 (figure 7*b*) is distinguished by its high values of radial velocity close to the flat surface and high wall shear stress. Wall vorticity is seen to increase and then decrease as one moves out radially. The suction caused by the jet induces a slight radially inward velocity at the tube exit and everywhere except close to the wall. This may also be seen from figure 4(*c*).

The corresponding axial velocity profiles at various radial locations are shown in figure 8. At the low value of $Re = 1$, axial velocity under the jet is seen to decrease rapidly even before the flat surface is approached (figure 8*a*). This is not the case at $Re = 1000$ due to strong axial convection as may be seen from figure 8(*b*).

A comparison is made in figure 9(*a*) between the velocity profile obtained at $R = 10$ (for $H = 4$ and $Re = 1000$) and the similarity solution due to Glauert. Since there is an undetermined constant, F, in the similarity solution of the boundary-layer equations, direct comparison is not possible. However, the same constant is involved in the transformation of all the variables and one can check the value of this constant for consistency as obtained from two different variables. For the case of $H = 4$, and

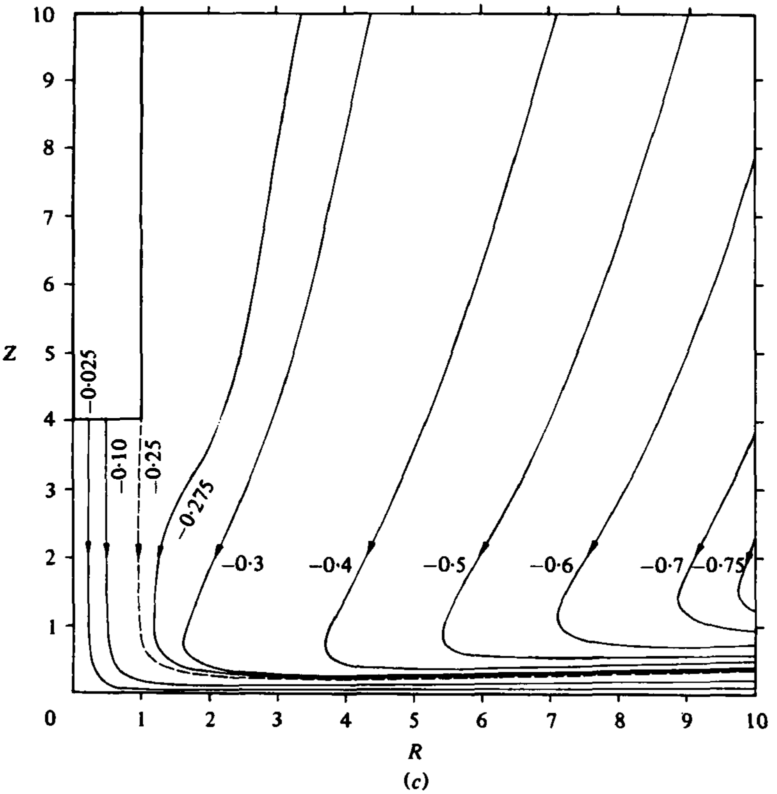

FIGURE 4. Streamlines, $H = 4$. Parabolic tube exit-velocity profile. (a) $Re = 1$; (b) $Re = 25$; (c) $Re = 1000$.

$Re = 1000$, $(F/\nu^3 a_0)^{\frac{1}{4}}$ turned out to be 4297 when the peak velocity of 0·1172 was matched with the maximum value of $f' = 0{\cdot}315$ from the similarity solution. The same constant turned out to be 4274 when the location of this peak velocity at $Z = 0{\cdot}385$ was matched with a value 2·029 of η_1, the length measured vertically from the wall in the similarity solution. In figure 9(*a*) the similarity solution is scaled to equate the peaks and the location of these peaks is seen to be in very good agreement. The two profiles agree well except away from the wall. The similarity solution was obtained assuming that as $\eta_1 \rightarrow \infty$, the radial velocity goes to zero without attaining negative values. In the present study this is not true since the jet draws the fluid radially inward.

A further comparison is made between the solution obtained and the axisymmetric stagnation point flow solution (see, for example, Schlichting 1979). The constant appearing in the stagnation-flow solution was determined at the stagnation point by equating the gradients of the wall shear stress for the two solutions at the stagnation point. This constant was then employed to compare the velocity profiles at $R = 0{\cdot}1$ and $R = 0{\cdot}3$ in figure 9(*b*). It is clear from the plots that comparison is good only in a small region and the agreement between the axial velocities is slightly better than that between the radial velocities.

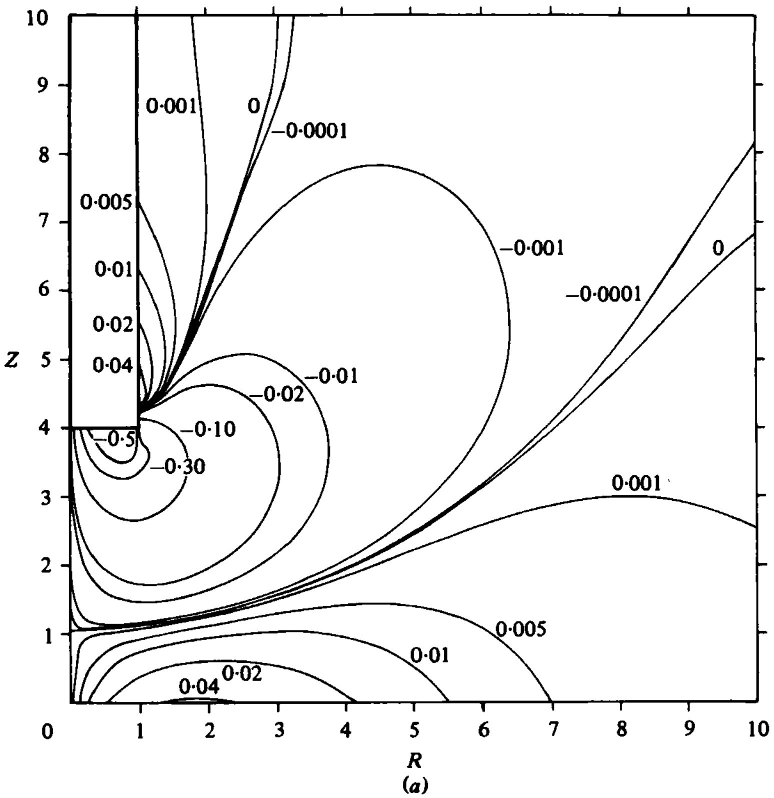

Caption for figure 5(a) on p. 226.

4.3. *Wall shear stress*

Non-dimensional wall shear stress $\tau_w/(4\rho\bar{u}^2)$ is plotted in figure 10(*a*) along the radial co-ordinate for $H = 4$ and $Re = 1, 5, 25, 100, 1000$ and 2000. The velocity profile at the tube exit is assumed to be parabolic as before. The shear stress is zero at $R = 0$ (stagnation point flow) and approaches zero asymptotically for large R. Hence one can expect the shear stress to reach a peak and then decrease as indicated in figure 10 (*a*). For $Re = 1$, the peak value occurs around $R = 1{\cdot}8$, i.e. outside the $R = 1$ circle defining the vertical projection of the tube on the target plane. When the Reynolds number of the flow increases, the location of the peak value of the wall shear stress gradually moves inward toward $R = 0{\cdot}85$. When the Reynolds number is increased from 1 to 5, the value of the non-dimensional shear stress decreases. This is not unusual and happens in several other laminar flows such as flow over a flat plate or flow through a tube. However, a further increase in Re leads to an increase in the peak value of the non-dimensional shear stress. A look at the streamline patterns in figure 4 indicates that this is due to the growth in the size of the eddy and its being pushed downwards. Beyond a value of about 100, an increase in Reynolds number leads to a decrease in the peak value of the nondimensional shear stress. For high values of Reynolds number and away from the tube, all the dimensionless shear stress curves come closer together, with values at higher Re being slightly higher. Away from the tube, for high Reynolds numbers, all curves get closer together, with the values at higher Reynolds numbers being slightly higher.

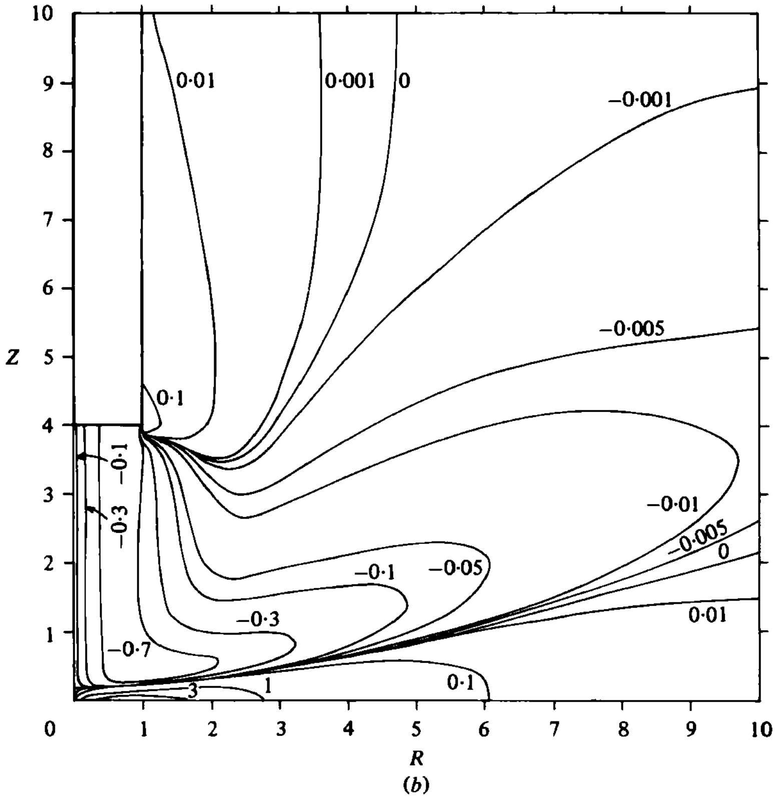

FIGURE 5. Vorticity contours, $H = 4$. Parabolic tube exit-velocity profile. (a) $Re = 1$; (b) $Re = 100$.

Similar plots are shown in figure 10 (b) for the case when the velocity profile at the tube exit is almost flat as indicated in § 2 (b). A substantial decrease in the shear stress from that in figure 10 (a) for the parabolic velocity profile is seen, especially close to the peak. The peak also occurs farther away from the axis. These results are to be expected since the momentum flux is reduced to $\frac{3}{4}$ of the value for a parabolic velocity profile and is more uniformly distributed over the tube cross-section.

The peak value of the non-dimensional shear stress is plotted as a function of Re in figure 11. Computations are done for several values of Reynolds number for the case of $H = 4$ and parabolic exit velocity profile. Flow cases of $H = 3$ with parabolic exit velocity profile and of $H = 4$ with flat exit velocity profile are also shown. Bringing the tube closer to the plane increases the peak wall shear stress and shifts the location of the peak closer to the axis, especially more so at lower values of Re. For the same value of H, the flat velocity profile leads to substantially lower peak values of the shear stress.

It is interesting to compare the present results with those obtained by Saad *et al.* (1977) for the axisymmetric impinging jet confined between two plates. The maximum values of wall shear stress $\tau_w/4\rho\bar{u}^2$ from Saad *et al.* are available for $H = 16$ whereas the present results are for $H = 4$. This does not permit a direct comparison. However, some interesting conclusions can be drawn. Values of $\tau_w/4\rho\bar{u}^2$ obtained in the present study and those obtained by Saad *et al.* are listed in table 2 for three values of Re and for parabolic and flat tube exit velocity profiles. For a high value of $Re = 1960$ and

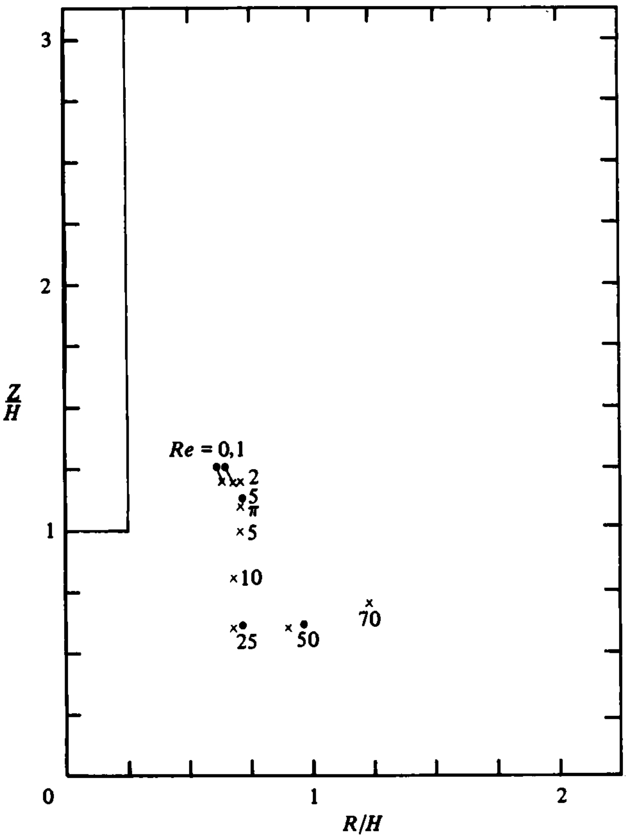

FIGURE 6. Eddy centre location. ×, $H = 4$; ⊗, $H = 3$. Parabolic tube exit-velocity profile.

parabolic exit-velocity profile the two values are very close. As the Reynolds number is decreased the maximum value of the non-dimensional shear stress $\tau_w/4\rho\bar{u}^2$ obtained by Saad *et al.* is lower, mainly due to a higher value of $H = 16$. This is consistent with figure 11. Moreover, this influence is more pronounced for the case of flat exit-velocity profile. Further, the study of Saad *et al.* as well as the present study indicate a concave upwards curve of wall shear stress close to the stagnation point (figure 10*b*) when the exit-velocity profile is flat.

4.4. *Pressure and pressure gradient*

The non-dimensional radial pressure gradient along the wall is plotted for several Reynolds numbers in figure 12 for the case of $H = 4$ and parabolic exit-velocity profile. The pressure gradient is zero at $R = 0$ and rapidly decreases to a minimum and then increases. At larger radial distances, there is an area of small positive pressure gradient, especially at higher values of Re. The pressure gradient approaches zero as R increases. The peak value of the magnitude of the pressure gradient is reached within one radius and is located closer to the stagnation point than the peak wall shear stress. The peak value of this non-dimensional pressure gradient is indicated in figure 13 as a function of Re for $H = 4$ and $H = 3$ with parabolic exit-velocity profile, and for $H = 4$ with a flat exit-velocity profile. The pattern is somewhat similar to that of the maximum wall

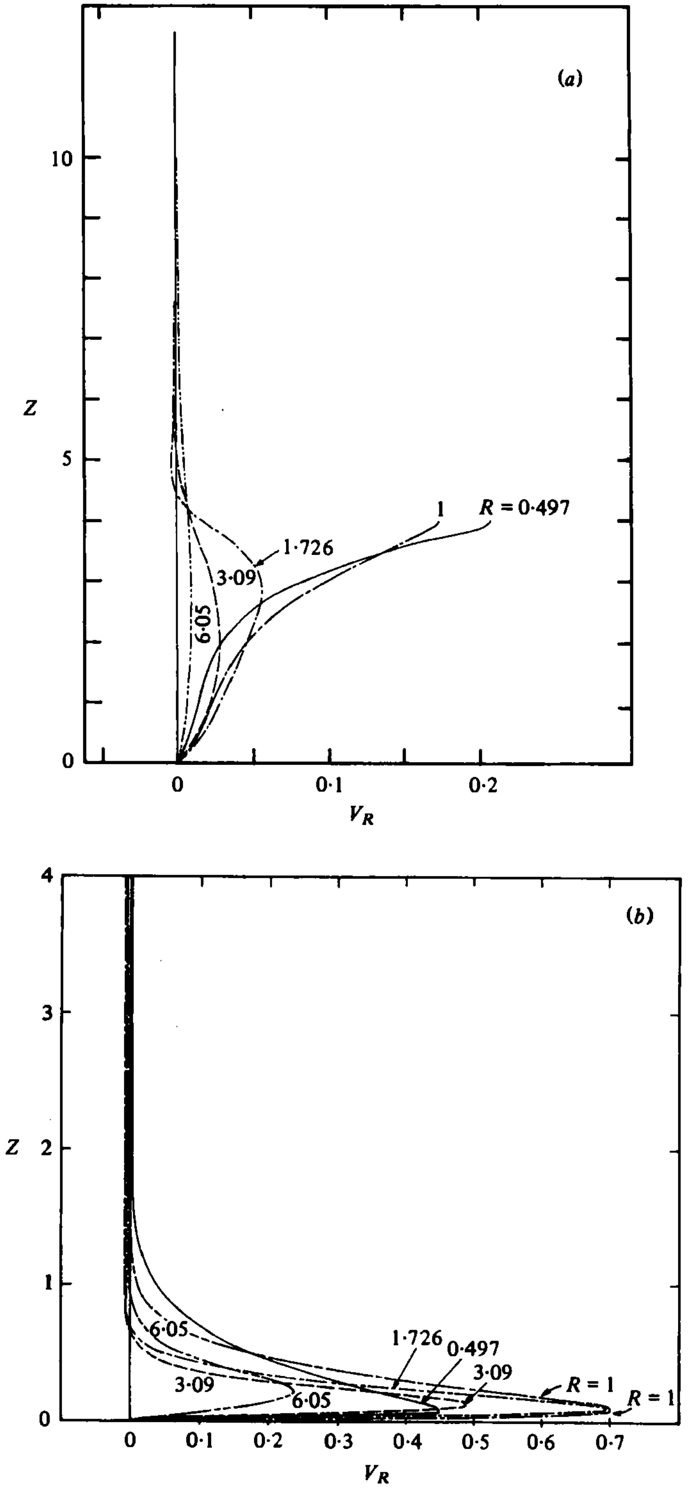

FIGURE 7. Radial velocity profiles, $H = 4$. Parabolic tube exit-velocity profile. (a) $Re = 1$; (b) $Re = 1000$.

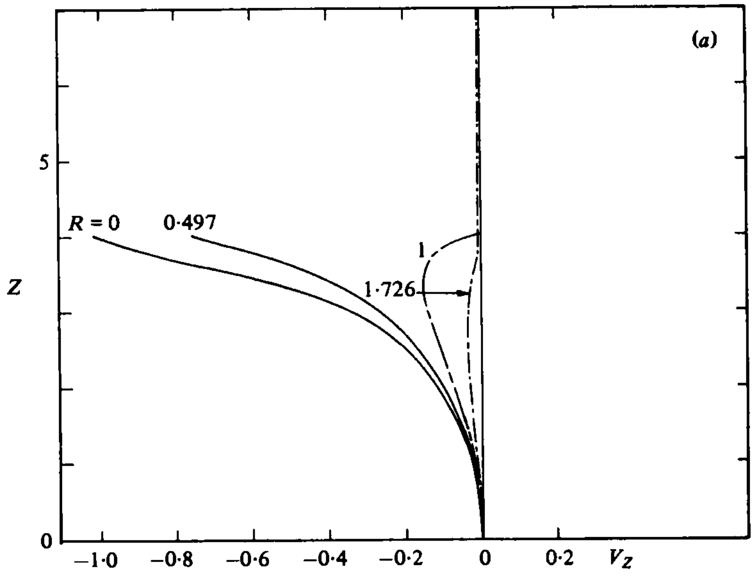

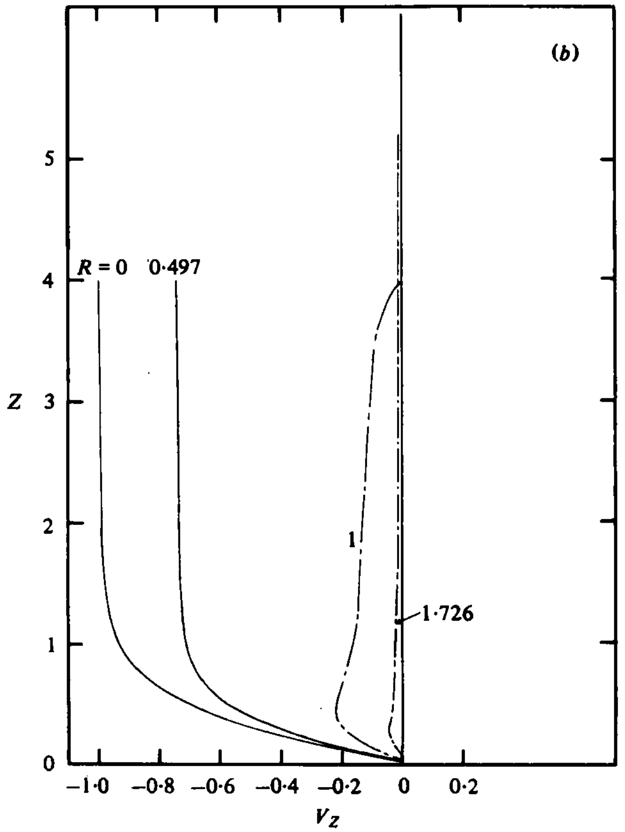

FIGURE 8. Axial velocity profiles, $H = 4$. Parabolic tube exit-velocity profile. (*a*) $Re = 1$; (*b*) $Re = 1000$.

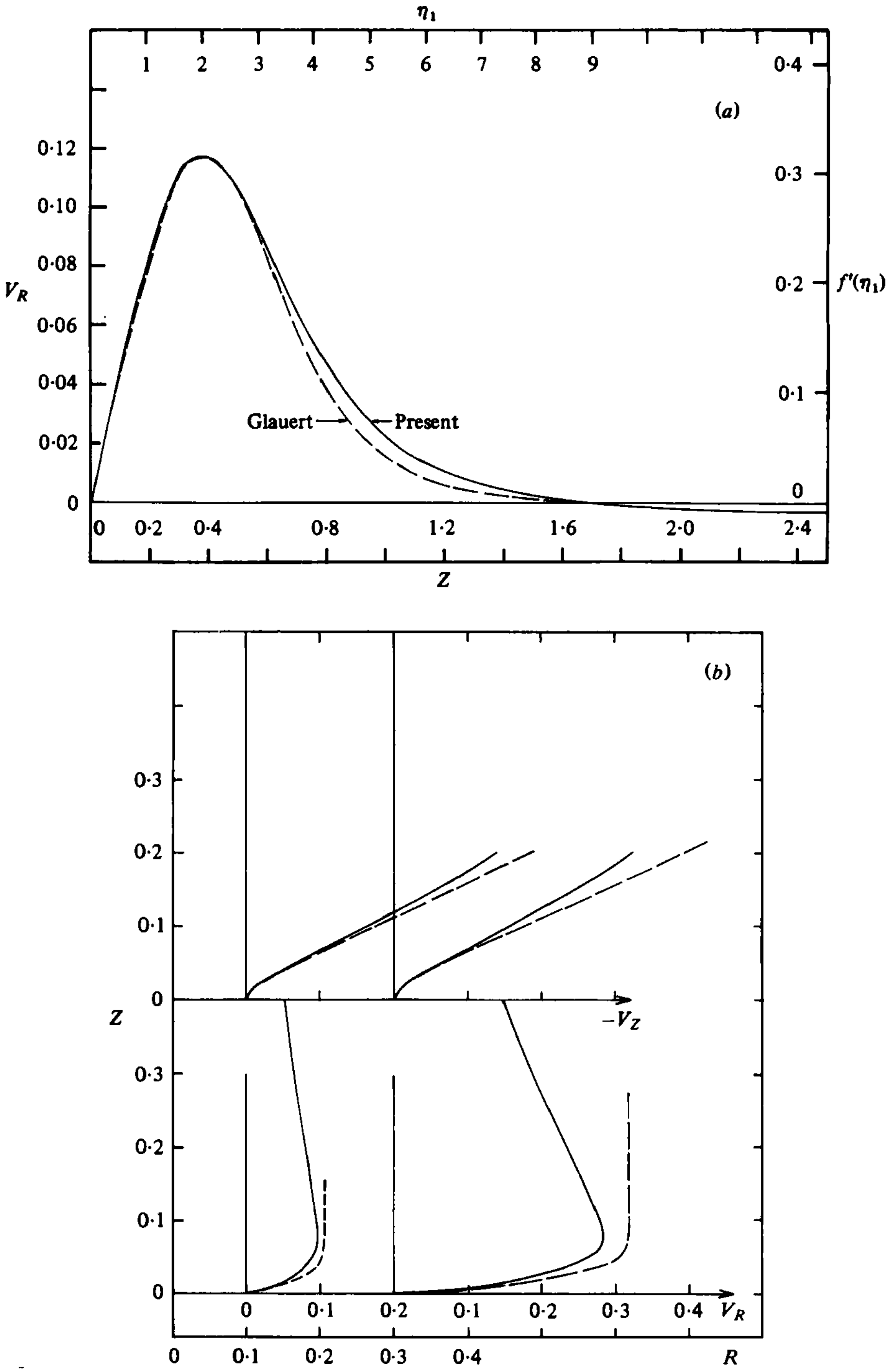

FIGURE 9. (*a*) Comparison with the similarity solution due to Glauert, $H = 4$, $Re = 1000$. (*b*) Comparison with the stagnation flow solution, $H = 4$, $Re = 1000$. $R = 0{\cdot}1$, $0{\cdot}3$. — — —, stagnation flow solution; ——, present results.

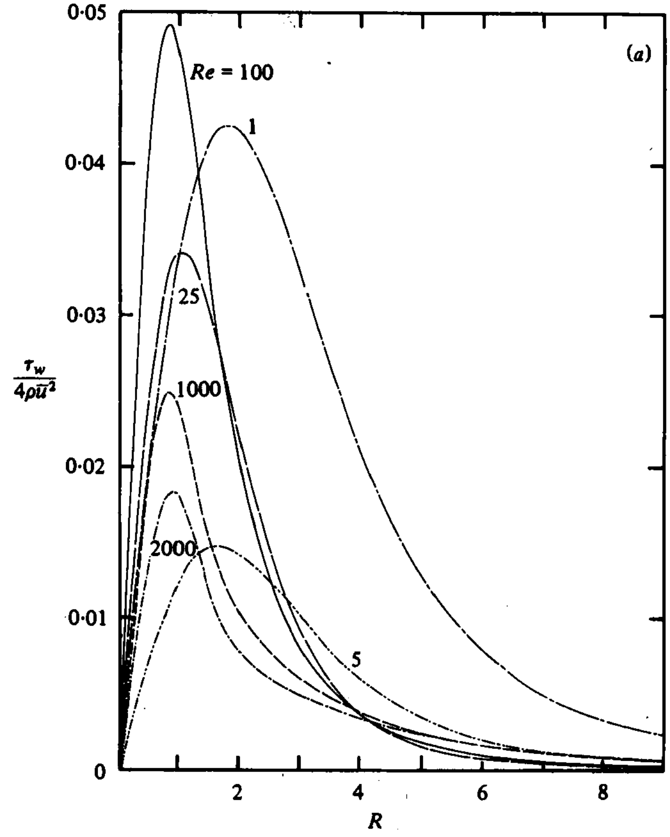

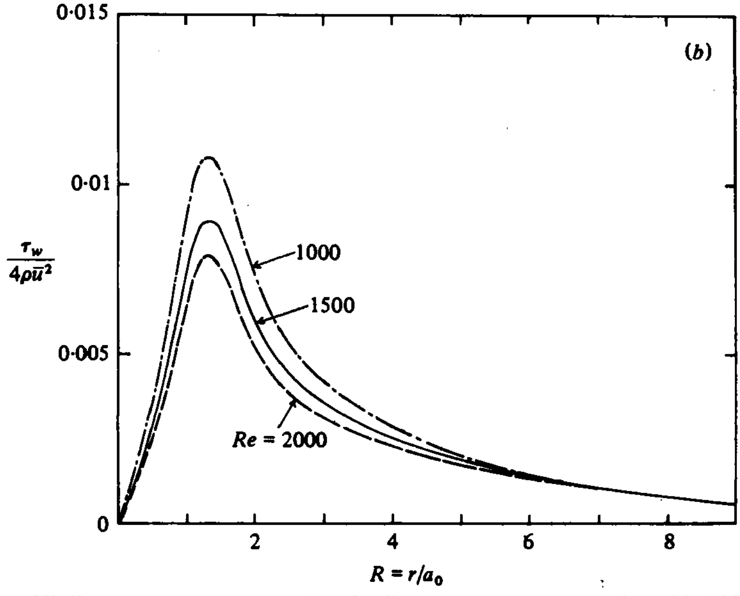

FIGURE 10. Wall shear stress distribution for $H = 4$. (*a*) $Re = 1, 5, 25, 100, 1000, 2000$. Parabolic tube exit-velocity profile. (*b*) $Re = 1000, 1500, 2000$. Flat tube exit-velocity profiles.

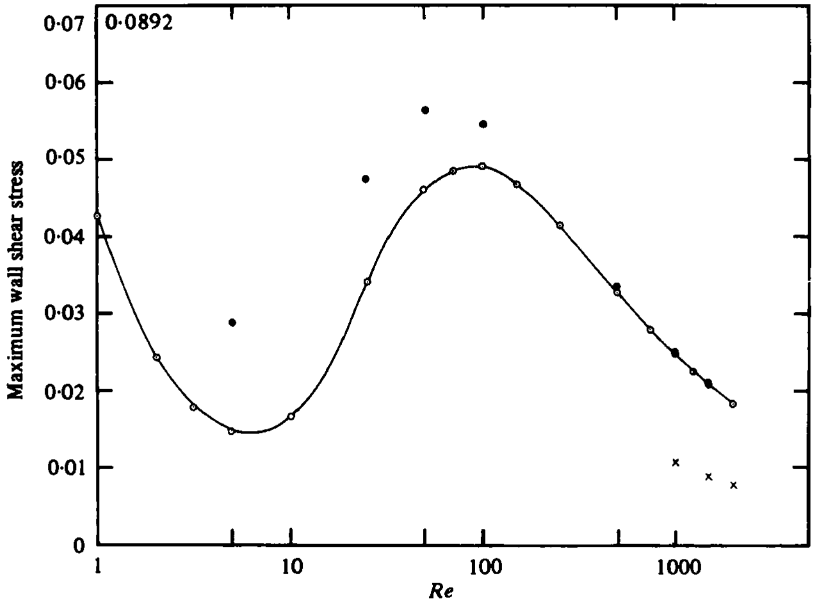

FIGURE 11. Maximum value of wall shear stress as a function of Reynolds number. Parabolic tube exit-velocity profile: ⊙, $H = 4$; ●, $H = 3$. Flat tube exit-velocity profile: ×, $H = 4$.

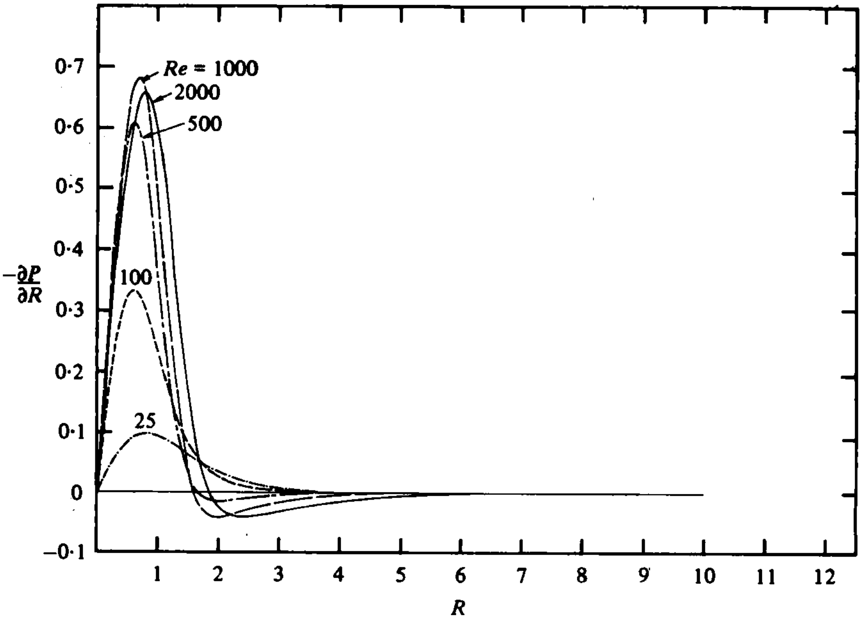

FIGURE 12. Pressure gradient $\partial P/\partial R$ distribution on the wall, parabolic tube exit-velocity profile for $H = 4$ and $Re = 25, 100, 500, 1000, 2000$.

	Parabolic exit-velocity profile		Flat exit-velocity profile	
	$H = 4$	$H = 16$	$H = 4$	$H = 16$
Re	Present	Saad *et al.*	Present	Saad *et al.*
450	0·034	0·0262	—	—
950	0·0253	0·0230	0·011	0·080
1960	0·0184	0·0189	0·0057	0·0044

TABLE 2. Comparison of the maximum values of $\tau_w/4\rho\bar{u}^2$ with those from Saad *et al.* (1977).

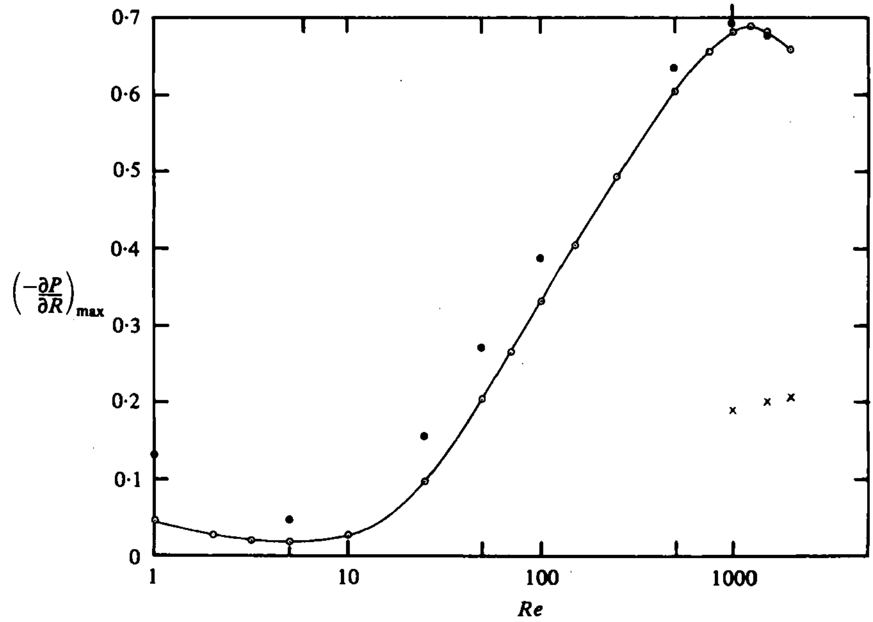

FIGURE 13. Maximum value of $(-\partial P/\partial R)$ on the wall as a function of *Re*. Parabolic tube exit-velocity profile: ○, $H = 4$; ●, $H = 3$. Flat exit-velocity profile: ×, $H = 4$.

shear stress indicated in figure 11. Bringing the tube closer to the wall increases the magnitude of the peak and a flat velocity profile at the tube exit leads to a substantial decrease in the peak. The value of the non-dimensional pressure at the stagnation point, with reference zero at a point far away, is indicated as a function of *Re* in figure 14.

5. Concluding remarks

The steady state Navier–Stokes equations have been solved numerically for two different tube exit-velocity profiles and for two different nozzle heights for the problem of an axisymmetric jet impinging on a target plane. The entire range of laminar flow is covered for the case of $H = 4$.

It may be of interest to gain some idea as to when one may expect the flow to become transitional. Chun & Schwarz (1967) examined the stability of the two-dimensional wall jet and found a critical value of Reynolds number Re_δ based on the boundary-layer thickness δ and the maximum radial velocity to be about 57. Similarly, Tsuji &

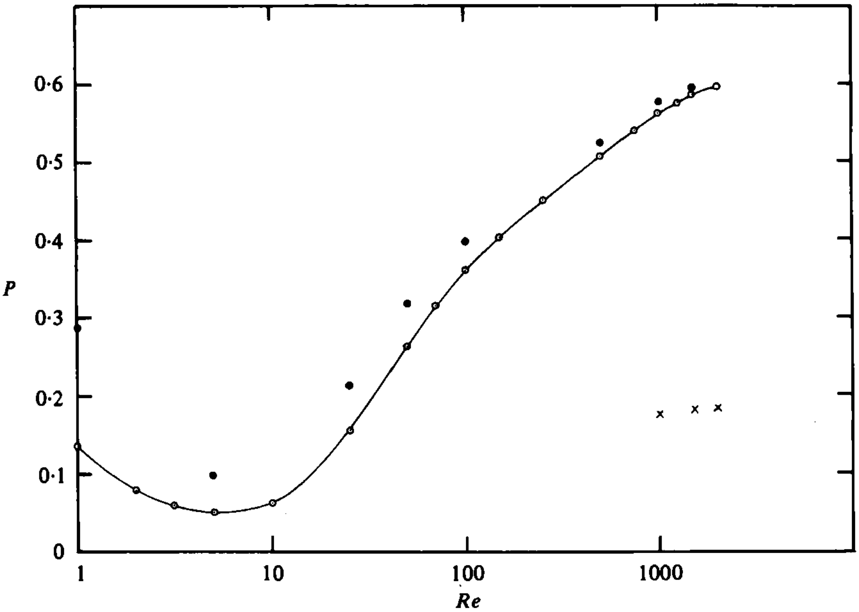

FIGURE 14. Stagnation point pressure P as a function of Re ($P = P_0 - P_\infty$). Parabolic tube exit-velocity profile: ○, $H = 4$; ●, $H = 3$. Flat exit-velocity profile: ×, $H = 4$.

Morikawa (1979) showed that an axisymmetric wall jet becomes unstable at a Reynolds number Re_δ of about 68. In case of similarity solution, Re_δ drops off as $R^{-\frac{1}{4}}$. In our computations the values of Re_δ were about 10 and 85 at the boundary $R = 10$ for $Re = 100$ and 1000, respectively. Thus, it is unlikely that the flow will remain laminar everywhere in the higher Reynolds-number range considered in this study. However, these results should help toward a fuller understanding of the physics of the problem. Our experiments, in which the signal from a hot-film wall shear probe was viewed on an oscilloscope, indicated spikes characteristic of turbulence around $Re = 1600$ when the tube exit was 4 radii above the plane ($H = 4$) and the velocity profile at the tube exit was parabolic.

The presence of a toroidal eddy at low Reynolds numbers is interesting and does not seem to have been noticed before. The maximum wall shear stress is strongly influenced by the size and location of the eddy. In the laminar flow, the non-dimensional shear stress, $\tau_w/(4\rho\bar{u}^2)$, generally decreases if Re is increased. This is observed for $Re < 5$ in the present study. However, for $Re > 5$ a larger amount of fluid is set into circulation closer to the wall. This leads to an increase in the wall shear stress. The usual behaviour of a decrease in $\tau_w/(4\rho\bar{u}^2)$ with an increase in Re occurs for $Re > 100$, because for these larger values of Re the eddy does not appear. Similar influences are felt on other flow quantities.

When the velocity profile is flat, the jet contains smaller amounts of momentum and kinetic energy for the same mass flux compared with that of a jet with a parabolic velocity profile. Moreover, the momentum and kinetic energy are distributed uniformly over the cross-section. This results in lower values of peak shear stress on the wall. This result led to an interesting observation in our experiments with the canine endothelial tissue (Vaishnav *et al.* 1978), where laminar and turbulent jets were used to erode the tissue. When the Reynolds number was in the range of 2000 to 2400, and the flow was turbulent, the jet was found to be less damaging than one would expect on the basis of the shear stress values for a laminar flow with a parabolic tube exit-velocity profile. This is believed to be partially due to the turbulent jet having a flatter velocity profile and consequently a lower mean input momentum, and partially due to the lower flow velocities resulting from turbulent diffusive action. These factors perhaps more than compensated for the increase in the wall shear stress due to turbulence.

Finally, we draw attention to the technique by which the boundary condition at the boundary $R = 10$ was handled. This technique may prove to be useful elsewhere.

We thank Professors H. B. Atabek and C. von Kerczek for reading the manuscript critically. Support of PHS grants HL-15270 and HL-12083 and NSF grant ENG760-02911 is gratefully acknowledged.

REFERENCES

BAINES, W. D. & KEFFER, J. F. 1976 Shear stress and heat transfer at stagnation point. *Int. J. Heat Mass Transfer* **19**, 21–26.

BAJURA, R. A. & SZEWCZYK, A. A. 1970 Experimental investigation of a laminar two-dimensional plane wall jet. *Phys. Fluids* **13**, 1653–1664.

BAKKE, P. 1957 An experimental investigation of a wall jet. *J. Fluid Mech.* **2**, 467–472.

BELTAOS, S. & RAJARATNAM, N. 1974 Impinging circular turbulent jets. *J. Hydraulics Div. Proc. A.S.C.E.* **100** (HY10), 1313–1328.

BRADBURY, L. J. S. 1972 The impact of an axisymmetric jet onto a normal ground. *Aero. Quart.* **23**, 141–147.

BRADSHAW, P. & LOVE, E. M. 1961 The normal impingement of a circular air jet on a flat surface. *Aero. Res. Counc. R. & M.* 3205.

CHUN, D. H. & SCHWARZ, W. H. 1967 Stability of the plane incompressible viscous wall jet subjected to small disturbances. *Phys. Fluids* **10**, 911–915.

DESHPANDE, M. D., GIDDENS, D. P. & MABON, R. F. 1976 Steady laminar flow through modelled vascular stenoses. *J. Biomech.* **9**, 165–174.

FRY, D. L. 1973 Responses of the arterial wall to certain physical factors. *Atherogenesis: Initiating factors*. CIBA Foundation Symp. Vol. 12, pp. 93–125. Elsevier.

GARDON, R. & AKFIRAT, J. C. 1966 Heat transfer characteristics of impinging two-dimensional air jets. *J. Heat Transfer* **88**, 101–108.

GLAUERT, M. B. 1956 The wall jet. *J. Fluid Mech.* **1**, 625–643.

GOSMAN, A. D., PUN, W. M., RUNCHAL, A. K., SPALDING, D. B. & WOLFSHTEIN, M. 1969 *Heat and Mass Transfer in Recirculating Flows*. Academic.

KAMOI, A. & TANAKA, H. 1972 Measurements of wall shear stress, wall pressure and fluctuations in the stagnation region produced by oblique jet impingement. In *Fluid Dynamic Measurements in the Industrial and Medical Environment* (ed. D. Cockrell), vol. 1, pp. 217–227. Leicester University Press.

LESTER, W. G. S. 1961 The flow past a pitot tube at low Reynolds numbers. *Aeronaut. Res. Counc. Rep. Memo.* 3240.

OJHA, S. K. & GOLLAKOTA, S. 1977 Jet impingement on a curved surface. *A.I.A.A. J.* **15**, 453–454.

PLOTKIN, A. 1970 A second-order correction to the Glauert wall jet solution. *A.I.A.A. J.* **8**, 188–189.

POREH, M., TSUEI, Y. G. & CERMAK, J. E. 1967 Investigation of turbulent radial wall jet. *J. Appl. Mech.* **34**, 457–463.

SAAD, N. R., DOUGLAS, W. J. M. & MUJUMDAR, A. S. 1977 Prediction of heat transfer under an axisymmetric laminar impinging jet. *Ind. Engng Chem., Fundam.* **16**, 148–154.

SCHLICHTING, H. 1979 *Boundary Layer Theory*. McGraw-Hill.

STRAND, T. 1962 Inviscid-incompressible-flow theory of static two-dimensional solid jets in proximity to the ground. *J. Aero-space Sci.* **29**, 170–173; 184.

TANI, I. & KOMATSU, Y. 1964 Impingement of a round jet on a flat surface. *Proc.* 11*th Int. Cong. Appl. Mech., Munich, Germany*, 672–676.

TETERVIN, N. 1948 Laminar flow of a slightly viscous incompressible fluid that issues from a slit and passes over a flat plate. *N.A.C.A. Tech. Note* 1644.

TSUJI, Y. & MORIKAWA, Y. 1979 Linear stability of a radial wall jet. *Aero. Quart.* **30**, 544–558.

VAISHNAV, R. N., ATABEK, H. B. & PATEL, D. J. 1978 Properties of intimal layer and adjacent flow. *J. Engng. Mech. Div. Proc. A.S.C.E.* **104**, 67–77.

VAN HEININGEN, A. R. P., MUJUMDAR, A. S. & DOUGLAS, W. J. M. 1976 Numerical prediction of the flow field and impingement heat transfer caused by a laminar slot jet. *J. Heat Transfer* **98**, 654–658.

WOLFSHTEIN, M. 1970 Some solutions of the plane turbulent impinging jet. *Trans. A.S.M.E.* D, *J. Basic Engng* **92**, 915–922.